



**HAL**  
open science

## **Co<sub>3</sub>O<sub>4</sub>-MnO<sub>x</sub> oxides supported on SBA-15 for CO and VOCs oxidation**

S Todorova, J L Blin, A Naydenov, Lebeau Bénédicte, H Kolev, P. Gaudin, A Dotzeva, R Velinova, D Filkova, I Ivanova, et al.

### ► **To cite this version:**

S Todorova, J L Blin, A Naydenov, Lebeau Bénédicte, H Kolev, et al.. Co<sub>3</sub>O<sub>4</sub>-MnO<sub>x</sub> oxides supported on SBA-15 for CO and VOCs oxidation. *Catalysis Today*, 2020, 357, pp.602-612. <10.1016/j.cattod.2019.05.018>. <hal-03060157>

**HAL Id: hal-03060157**

**<https://hal.science/hal-03060157v1>**

Submitted on 13 Dec 2020

**HAL** is a multi-disciplinary open access archive for the deposit and dissemination of scientific research documents, whether they are published or not. The documents may come from teaching and research institutions in France or abroad, or from public or private research centers.

L'archive ouverte pluridisciplinaire **HAL**, est destinée au dépôt et à la diffusion de documents scientifiques de niveau recherche, publiés ou non, émanant des établissements d'enseignement et de recherche français ou étrangers, des laboratoires publics ou privés.



HAL Authorization

## **Co<sub>3</sub>O<sub>4</sub>-MnO<sub>x</sub> oxides supported on SBA-15 for CO and VOCs oxidation**

S. Todorova<sup>1\*</sup>, J. L. Blin<sup>2</sup>, A. Naydenov<sup>3</sup>, B. Lebeau<sup>4</sup>, H. Kolev<sup>1</sup>, P. Gaudin<sup>2</sup>, A. Dotzeva<sup>1</sup>, R. Velinova<sup>3</sup>, D. Filkova<sup>1</sup>, I. Ivanova<sup>1</sup>, L. Vidal<sup>4</sup>, L. Michelin<sup>4</sup>, L. Josien<sup>4</sup>, K. Tenchev<sup>1</sup>

<sup>1</sup>*Institute of Catalysis, Bulgarian Academy of Sciences, Acad. G. Bonchev St., Bldg. 11, 1113 Sofia, Bulgaria*

<sup>2</sup>*Université de Lorraine/CNRS, L2CM, UMR7053, F-54506 Vandoeuvre-lès-Nancy cedex, France*

<sup>3</sup>*Institute of General and Inorganic Chemistry, Bulgarian Academy of Sciences, Acad. G. Bonchev St., Bldg. 11, 1113 Sofia, Bulgaria*

<sup>4</sup>*Université de Haute Alsace (UHA)/CNRS, IS2M, UMR 7361, 68093 Mulhouse cedex, France*

### **Abstract**

Mono- and bi-component cobalt and manganese samples were prepared by “two-solvent” technique using SBA-15 as a support. The obtained materials were characterized by SAXS (Small angle X-Ray scattering), N<sub>2</sub> adsorption-desorption, X-ray diffraction, TEM (Transmission Electron Microscopy), X-ray photoelectron spectroscopy (XPS), TPR (Temperature-programmed reduction) and O<sub>2</sub>-TPD (Oxygen Temperature-programmed desorption). The catalytic properties were tested in the complete oxidation of propane, *n*-hexane, and carbon monoxide.

The modification of the SBA-15 materials with Co, Mn or simultaneously with both cobalt and manganese does not change significantly the mesoporous structure, however its pores are partially blocked by the oxides, resulting in the decrease in the specific surface area and in the pore volume. In the case of mono component Co-SBA-15, the clusters of Co<sub>3</sub>O<sub>4</sub> are on the surface and they are partially located inside the pore system of SBA-15 while for Mn-SBA-15 sample, the oxide phases preferentially fill up the channels of SBA-15 forming nanowires. The mixed oxide nanowires are formed in the channels of CoMn-SBA-15 material along with small nanoparticles, aggregated outside of the channels.

The mesoporous structure and morphology of SBA-15, type of oxide phases and the size of the oxide particles remain almost unchanged after tests in reaction of complete *n*-hexane oxidation and this is valid for all studied samples. The observed resistance towards agglomeration can be attributed to the mesoporous structure. On the other hand, after reaction the surface concentration of different cobalt and manganese species undergoes significant changes, except for the sample with equimolar Co:Mn ratio.

The most active catalyst among bi-component Co-Mn samples in all studied reactions, is the catalyst where the Co:Mn molar ratio is 1:0.5, which can be explained by the formation of finely divided oxides, thus ensuring highest reducibility and oxygen mobility.

*Key words:* SBA-15; Co-Mn-SBA-15; *n*-hexane combustion; propane oxidation, CO oxidation

## ***Introduction***

Abatement of volatile organic compounds (VOCs) and CO contents in the waste gases is an important task for environmental protection and odour control. There exist a great number of successful commercial catalysts developed for CO and VOC complete oxidation. Nevertheless, there still exists a demand for developing some new optimized catalysts with increased efficiency of mass and heat transfer and which should not contain any noble metals. Transition metal oxides have shown some very good catalytic activities in oxidation reactions, but their main drawback is the deactivation of the catalysts as result of sintering. Among all studied metal oxides the most active single metal oxides are those of Cu, Co, Mn and Ni [1]. Manganese and cobalt containing catalysts are less expensive and demonstrate high activity in CO and VOCs complete oxidation [2]. The catalytic properties of MnOx-based catalysts are attributed to the ability of manganese to form oxides having different oxidation states and their high oxygen storage capacities (OSC) [3, 4]. The Co<sub>3</sub>O<sub>4</sub>-based catalysts offer the best balance between cost and catalytic activity since their behaviour is often very close to that of expensive noble metals and its selectivity to CO<sub>2</sub> is higher, when comparing them to other transition metal oxide catalysts (such as Mn<sub>2</sub>O<sub>3</sub> or V<sub>2</sub>O<sub>5</sub>) [5, 6, 7, 8]. Cobalt oxide is reported to be quite promising among the metal oxides used for preparation of supported catalysts for the removal of CO even at room and lower temperatures [9]. Wang et al. [10] determined the key factors for the extraordinarily high catalytic activity of Co<sub>3</sub>O<sub>4</sub>-based catalysts: CO adsorption strength, the barrier of CO reacting with the lattice oxygen and the redox properties of Co<sub>3</sub>O<sub>4</sub>. There are investigations, according to which the cobalt - based catalysts with high cobalt dispersion degrees are active in methane [11], propane [12] toluene [13, 14] removal. It is generally observed that the morphology or the crystal plane of Co<sub>3</sub>O<sub>4</sub> nanocrystals can remarkably alter their catalytic performance [5]. The combination of Co<sub>3</sub>O<sub>4</sub> and other different oxides such as CeO<sub>2</sub>, ZrO<sub>2</sub>, Al<sub>2</sub>O<sub>3</sub>, etc. often affects the textural, morphological, redox, acidic and basic properties, as well as the catalytic activity. Cobalt-manganese oxides demonstrate high catalytic efficiency in oxidation of CO, benzene, toluene, 2-propanol, propane and other pollutants [15, 16]. In our previous study [17] we established that the combination between cobalt and manganese oxides changed significantly the activity in the *n*-hexane and methane oxidation [18] and this activity depended on the sequence of cobalt and manganese introduction to the catalyst sample.

The main drawback of the transition metal oxides-based catalysts is their deactivation as a result of an aggregation. The problem could be overcome by applying novel preparation methods and application of supports with some new properties, as those demonstrated by nanostructured mesoporous oxides. The mesoporous supports would give rise to well-dispersed and stable metal particles, supplying abundant pores and large specific surface areas, thus possessing a great potential in further improvement of the catalytic performance. SBA-15, MCM-41, MCM-48, KIT-6 are used as supports for noble and transition metal catalysts for oxidation of CO and VOC. SBA-15 has attracted much interest since it possesses a regular hexagonal array of pores with uniform diameter, a very high specific surface area and high pore volume. It is also inert and stable at elevated temperature and has good mechanical stability. Moreover, its surface can be easily functionalized [19]. Z. Xiao-Dong et al. summarized the recent results in the removal of volatile organic compounds by mesoporous silica materials and supported catalysts [20]. The strong effect of support pore topology on the formation of cobalt [13, 21], iron [22] and bi-component copper and ceria [23], manganese [24] nanoparticles hosted in mesoporous silicas type SBA-15 and KIT-6 are

illustrated in the investigation by Tsoncheva and co-authors. In their work [22] the modifications of SBA-15, KIT-5 and KIT-6 mesoporous silicas with different pore sizes with cobalt oxide was studied. It was established that the supports with larger mesopores facilitated the formation of easily reducible  $\text{Co}_3\text{O}_4$  spinel particles. However, the interconnectivity of the mesopores and the uniformity of the channel dimensions also had some influence on the catalytic activity, implying that mass-transfer effects occur, especially in the case of supports with cage-like mesopores. More homogeneously dispersed MnOx nanoparticles are formed on 2D-silica type SBA-15, while the more opened 3D-structure of KIT-6 provokes the formation of more highly exposed to the reactants manganese species [24]. To the best of our knowledge there are no reports concerning simultaneous modification of SBA-15 with both cobalt and manganese oxides.

As it was mentioned above in our previous investigations the combination between cobalt and manganese oxides changed significantly the activity in the *n*-hexane and methane oxidation [17, 18]. The present work is a continuation of our research efforts in the field of application of mixed Co-Mn oxide catalysts for the combustion of different VOC. The work is focused on the investigation of the structural and catalytic properties of series of mono-component cobalt and manganese and bi-component Co-Mn catalysts supported on SBA-15.

The selected test reactions are CO oxidation and combustion of propane and *n*-hexane. The specified volatile organic compounds are chosen because the propane is the main component in LPG (composed of primarily propane and butane) and *n*-hexane, because it is the component of many products related to industry and it participates in a radical chain reaction yielding compounds, which exist in the photochemical smog. CO is widespread and highly toxic gas, which requires its elimination in waste gases.

## ***2. Materials and methods***

### ***2.1. Catalysis preparation***

SBA-15 was synthesized by a sol-gel route according to a standard procedure in the presence of a triblock copolymer, Pluronic P123 [(EO)<sub>20</sub>(PO)<sub>70</sub>(EO)<sub>20</sub>], as structure-directing agent [25]. In a typical synthesis: 2.66 g of P123 were dissolved in 100 mL of a hydrochloric acid solution (1 M). Then, 4.17 g of TMOS, the inorganic precursor, were added and the mixture was stirred at room temperature for 30 min. Afterwards the solution was transferred into an autoclave and heated at 40 °C in the course of 24 h following by a heating at 100 °C for 48 h. The mesoporous silica material was obtained after surfactant extraction by ethanol lasting for 48 h using a Soxhlet apparatus. The powder was then dried up in vacuum overnight to achieve SBA-15 as a white powder.

Both single component (Co and Mn) as well as bi-component samples were prepared according to the “two-solvent” technique [26]. The SBA-15 material was first suspended in dry hexane, used as hydrophobic solvent. Then, a desired amount of metal nitrate was dissolved in distilled water, the quantity corresponding to the pore volume of SBA-15 determined by N<sub>2</sub> adsorption. This aqueous solution containing metal precursors was then added dropwise to the suspension. The gel was allowed to age for 2 h under vigorous stirring. The solid phase was recovered by filtration and dried up in air and then calcined for 3 h at 500°C in air atmosphere. The samples were denoted as Co-SBA-15, Mn-SBA-15, 1CoMn0.5SBA-15, 1Co1Mn-SBA-15, and 1Co2Mn-SBA-15, where the number represents the Mn and Co number of moles.

## 2.2. Catalyst samples characterization

The obtained materials were characterized by SAXS, N<sub>2</sub> adsorption-desorption, X-ray diffraction, SEM and TEM microscopy.

Small angle X-Ray scattering (SAXS) data were collected on a “SAXSess mc<sup>2</sup>” instrument (Anton Paar), using line-collimation system. This instrument is attached to an ID 3003 laboratory X-Ray generator (General Electric) equipped with a sealed X-Ray tube (PANalytical,  $\lambda$  Cu,  $K\alpha = 0.1542$  nm) operating at 40 kV and 50 mA. Each sample was introduced into a “Special Glass” capillary for liquids and liquid crystals ( $\Phi = 1.5$  mm and 2.0 mm for micellar solutions and liquid crystals, respectively), or between two sheets of Kapton® for materials, then placed inside an evacuated sample chamber, and exposed to X-Ray beam. Scattering of X-Ray beam was registered by a CCD detector (Princeton Instruments, 2084 x 2084 pixels array with 24 x 24  $\mu\text{m}^2$  pixel size) at 309 mm distance from the sample. Using SAXSQuant software (Anton Paar), the 2D image was integrated into one-dimensional scattering intensities  $I(q)$  as a function of the magnitude of the scattering vector  $q = (4\pi/\lambda) \sin(\theta)$ , where  $2\theta$  is the total scattering angle. Thanks to a translucent beam-stop allowing the measurement of an attenuated primary beam at  $q = 0$ , all measured intensities can therefore be calibrated by normalizing the attenuated primary intensity. Data were then corrected for the background scattering from the cell and for slit-smearing effects by a desmearing procedure from SAXSQuant software, using Lake method.

Nitrogen adsorption-desorption isotherms were carried out at  $-196$  °C within a wide relative pressure ( $P/P_0$ ) range varying from 0.010 to 0.995 with a volumetric adsorption analyzer TRISTAR 3000 manufactured by Micromeritics. Before measurements, the samples were outgassed under vacuum (pressure = 0.13 mBar) at 25 °C for 16 hours. The specific surface area of each sample was calculated by the Brunauer-Emmett-Teller (BET) method [25]. The pore diameter and the pore size distribution were determined from the adsorption branch of the corresponding isotherm using the Barret-Joyner-Halenda (BJH) method [28].

Wide angles X-Ray diffraction patterns were collected on a PANalytical MPD X'Pert Pro diffractometer operating with Cu  $K\alpha$  radiation ( $K\alpha=0.15418$  nm) equipped with an X'Celerator real-time multiple strip detector (active length= $2.12^\circ 2\theta$ ). The XRD powder patterns were collected at 25°C within the range  $3 < 2\theta < 70$ , step=  $0.017^\circ 2\theta$ , time/step=220s. The phases identification has been realised with the X'PertHighscore software (PANalytical) and the PDF-4+ 2018 database from the International Centre for Diffraction Data (ICDD).

Transmission Electron Microscopy (TEM) images, chemical analyses and electron diffraction of the samples were performed using a JEOL ARM200-CFEG microscope operating at 200 kV. Prior to the observation, the powder was dispersed into chloroform by ultrasonic treatment and a few drops of the suspension were deposited on the surface of a gold observation grid covered with a formvar or amorphous carbon film. The EDX analyses and chemical mappings were performed using a JEOL Centurio detector. The electron diffraction micrographs were acquired with a camera length of 300 mm.

X-ray photoelectron spectroscopy (XPS) was carried out using ESCALAB MkII (VG Scientific) electron spectrometer at a base pressure in the analysis chamber of  $5 \times 10^{-10}$  mbar (during the measurement it was  $1 \times 10^{-8}$  mbar), using Al $K\alpha$  X-ray source (excitation energy  $h\nu=1486.6$  eV). The pass energy of the hemispherical analyzer was 20 eV (because of its weak signal for Co2p 50 eV pass energy was used), 6 mm slit widths (entrance/exit). The instrumental resolution measured as the full width at a half maximum (FWHM) of the Ag3d5/2 photoelectron peak is 1 eV. The energy scale is calibrated with respect to the Si2p -

peak maximum at 103.3 eV for electrostatic charging. The processing of the measured spectra is described in [17, 18].

Temperature-programmed reduction (TPR) was carried out using a flow mixture of 10% H<sub>2</sub> in argon at a flow rate of 10 ml.min<sup>-1</sup> and a temperature ramp of 10 deg.min<sup>-1</sup> up to 700°C. Prior to the TPR experiments, the samples were treated in argon flow at 150°C for 1 h.

Oxygen-TPD data were obtained by using of oxygen gas analyser Teledyne Mod. 802 (paramagnetic principle). The samples (0.14 g) pre-treatment consisted of heating in flow of 5% O<sub>2</sub> in N<sub>2</sub> at 450°C for 6 hours, then cooling down to room temperature in the same gaseous mixture. The applied heating rate was 7.5 K. min<sup>-1</sup>, gas flow rate: nitrogen, 500 ml.min<sup>-1</sup>.

### 2.3. Catalytic activity

The catalytic properties were tested in the complete oxidation of propane, *n*-hexane and carbon monoxide.

The catalytic activity tests in CO oxidation reaction were carried out in a flow type of glass reactor at atmospheric pressure with a catalyst loading of about 0.5 cm<sup>3</sup> (fraction 0.25–0.31 mm). The gaseous mixture consisted of 1 vol. % CO, 10 vol.% O<sub>2</sub> and He for balance to 100 vol.%. External mass transfer limitations were minimized by operating at high gaseous hourly space velocities (GHSV) (60 00 h<sup>-1</sup>). The converted mixture analysis was performed by a HP5890 series II gas chromatograph equipped with a thermal conductivity detector (TCD) and Carboxen-1000 GC column.

Catalytic activity tests in the complete oxidation reactions of propane and *n*-hexane were performed using an integrated quartz micro-reactor and mass spectrometer analysis system (CATLAB, Hiden Analytical, UK). The converted gas mixture analysis was carried out using the mass-spectrometer of the CATLAB system and in addition to it the on-line analysis of CO/CO<sub>2</sub>/O<sub>2</sub> (Maihak, NDIR) and THC-FID (total hydrocarbon content with a flame ionization detector, Horiba). The check for possible formation of oxidized organics by-products was performed by GC - MS analyser, model AL7890A.

Reactant gases were supplied through electronic mass flow controller system. The catalysts (particle sizes of 0.3–0.6 mm) were held between plugs of quartz wool in a quartz tubular vertical flow reactor ( $\phi = 6$  mm). In order to maintain almost the same heat, released by the reaction for each hydrocarbon, propane ( $\Delta H = -2220.0$  kJ/mol) and *n*-hexane ( $\Delta H = -4163.7$  kJ/mol) inlet concentrations in synthetic air were kept at 2000 and 1000 ppm, respectively. The same GHSV as that for CO tests was used (60 000 h<sup>-1</sup>).

## 3. Results and Discussion

### 3.1. Characterization of catalyst samples

The characterization of all catalyst samples was done as prepared and after *n*-hexane oxidation.

#### 3.1.1. Characterization of the mesoporous catalysts

The SAXS pattern of the parent SBA-15 exhibits three lines at 10.7, 6.2 and 5.3 nm (Fig. 1A Supplementary data). They are characteristic of the (100), (110) and (200) reflections of the 2D-hexagonal arrangement of the mesoporous channels. SBA-15 exhibits a type IV isotherm (Fig. 1B Supplementary data), according to the IUPAC classification [29]. An H1 type of hysteresis loop, in which adsorption and desorption branches are steep, has been observed. The specific surface area and pore volume values are respectively 982 m<sup>2</sup>/g and

0.99 cm<sup>3</sup>/g. The pore diameter distribution determined by using the BJH method is quite narrow and it is centred at ca. 9.0 nm (Fig. 1C Supplementary data).

After the introduction and decomposition of the cobalt and/or manganese precursors the hexagonal mesopore ordering is still observed (Fig. 1A) but the  $d_{100}$  is slightly shifted towards lower values (from 10.7 to about 10.0 nm) and the intensity of the peaks decreases (Fig 1A). The  $d_{100}$  shift indicates shrinkage of the mesopores after calcination at 500°C to decompose the Co and Mn precursors, whereas the decrease in the intensity implies that some metal species fill up the mesopores of the SBA-15 [30]. More noticeable reduction in intensity is observed with the samples with a higher manganese content indicating that Mn most likely is responsible for filling up the mesopores. This fact is further confirmed by TEM images. The hexagonal structure is preserved after the reaction (Fig. 1B). There is no variation in the d-spacing values but it can be seen that the reflections are better resolved and that they present a higher intensity, in particular for the case of Mn-rich catalysts.

The TEM images of all materials (Fig. 2) are coherent with the presence of SBA-15 particles with well-ordered mesopores in a 2D hexagonal arrangement. Both Co-SBA-15 and Mn-SBA-15 show the presence of well dispersed large dark particles that are in contrast with the dark grey silica walls and the light grey voids of the pores (Fig. 2a-d). Dark particles more or less spherical are observed for Co-SBA-15 with an average size ranging 100 nm that is much larger than the diameter of the parent SBA-15 (Fig. 2a). At high magnification ordered channels could be distinguished on the large nanoparticles, which indicates that the large nanoparticles were inside the nanochannels and these are composed of small nanoparticles in adjacent channels due to the micropores in the walls of SBA-15 (Fig. 2b). Similar morphology was observed for Co<sub>3</sub>O<sub>4</sub> nanoparticles generated within the mesopores of SBA-15 in supercritical CO<sub>2</sub> and nitric acid as co-solvent [31]. When aggregates are being formed close to the particle surface, the formation of Co<sub>3</sub>O<sub>4</sub> outside the pores is also observed. In the case of Mn-SBA-15 dark nanowires along pores and images at high magnification indicate that they fill up the mesopores (Fig. 2c, d). For the mixed 1Co1Mn-SBA-15 material, a mixture of aggregated small nanoparticles in adjacent channels and nanowires is observed (Fig. 2 e, f).

The EDX analyses (Fig. 3) were performed with the all studied samples and Co and Mn element mapping confirmed the only presence of Co and Mn in the same phase in the two component catalysts.

The TEM observations after carrying out reaction (Fig 2 Supplementary data) were performed on the Co-SBA-15, Mn-SBA-15 and 1Co1Mn-SBA-15 materials. Among two-component Co-Mn sample the 1Co1Mn-SBA-15 was chosen for TEM study after reaction, due to the fact that the surface concentration of cobalt and manganese species changed insignificant and this gave us reason to assume that this sample would show the highest stability. In all cases the SBA-15 particles were observed partially broken. The morphologies of the Co and Mn nanoparticles are similar to those before reaction (Fig. 2 Supplementary data a-d). For mono component manganese sample, some aggregates of nanoparticles are coexisting with nanowires (Fig. 2 Supplementary data e, f). EDX analyses (Fig. 3 Supplementary data) were also performed and element mapping is coherent with the only presence of Co, Mn and mixed Co/Mn in Co-SBA-15, Mn-SBA-15 and 1Co1Mn-SBA-15 materials, respectively. EDX spectra were also recorded at low magnification by using SEM to determine the element composition (Table 1). The Co-SBA-15, Mn-SBA-15 and 1Co1Mn-SBA-15 materials have roughly the same composition before and after carrying out the reaction: about 7.3% of Co, 8.0 % of Mn, 3.5%Co/4.1%Mn, respectively.

Except a decrease in the nitrogen adsorbed volume, no significant change is noted in the adsorption branch of the isotherm (Fig 4A). In contrast to it the shape of the desorption branch indicates that some of the mesopores are blocked. After the introduction of the active metals a decrease both in the specific surface area and in the pore volume was observed (Table 2). Meanwhile, the pore size distribution (Fig. 5A) presents two components at about 7.0 nm and 9.0 nm, taking into account the error of the measurement. The smallest value is in accordance with the introduction of the metal species in the mesopores and their shrinkage upon calcination at 500°C and the second one reflects a mesopores blocking.

All the results reported above imply that the active metal oxides are confined inside the mesopores but also that some part of them is deposited at the entrance of the channels.

Figure 4B represents nitrogen adsorption-desorption analyses after the reaction. Based on the nitrogen adsorption-desorption analyses it can also be concluded that the feature of the isotherm is not significantly modified. We still have type IV isotherm, characteristic of mesoporous materials. A decrease in the specific area and in the mesopore volume is noticed (Table 2). Concerning the specific surface area, the decrease varies between 6.5 and 11% for the Co and for the mixed catalysts and it reaches 33% for the Mn-based catalyst. The latter sample also shows the highest decrease in the mesopore volume: 45% comparing with the other materials (between 9 and 15%). We can also observe a modification of the mesopore size distributions (Fig. 5B). Even if they are asymmetric, it seems that the component at about 9.0 nm disappears, while the other one at about 7.0 nm still persists. It can be assumed that during the reaction, which has been performed up to 500°C, the clogged mesopores shrink to reach a similar diameter than the ones filled by the metal oxides. The mesopore diameter after the reaction is in accordance with the one obtained for a bare SBA-15 calcined in this range of temperature [30]. The size of the mesopores containing the metal oxides is not significantly modified since their presence prevents the shrinkage. The metal oxides species seem to consolidate the mesoporous silica framework.

Based on the results from the applied instrumental methods it can be concluded that the modification of SBA-15 with Co and Mn does not change significantly the mesoporous structure of silica support. It can be supposed that the decrease in the specific BET surface area, pore volume and the insignificant modification of the adsorption-desorption curve shape is due to the partial pore blocking by cobalt and manganese oxide particles, which is confirmed also by TEM images. The most significant lowering of the surface area and pore volume is observed in the mono-component manganese sample, indicating that most of the oxide is located in the SBA-15 channels. As it is shown by the TEM images, the manganese oxide formed nanowires. Significant changes in the mesoporous structure and morphology are not observed after the reaction.

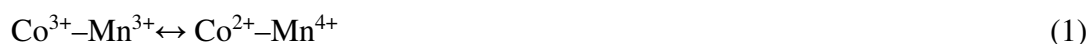
### *3.1.2. Characterization of the supported metal species*

The oxidation states of Co and Mn on the surface is examined by XPS. Fig. 4 from Supplementary data shows an example curve fitting of Co2p<sub>1/2</sub> (left-hand side) and Mn2p (right-hand side) core levels of investigated samples before the catalytic activity test. A peak in the energy range of 792-798 eV is measured for cobalt with defined binding energies (BEs) either of 794.9 eV (Co<sup>3+</sup>) or 795.9 eV (Co<sup>2+</sup>), respectively. The presence of Co<sup>2+</sup> ions in the cobalt-containing samples is confirmed by the presence of a peak with binding energy of 795.9 eV, together with the relatively intensive 3d→4s "shake-up" satellite with binding energy of 803-804 eV (Figure 4A Supplementary data). The Mn2p peaks are measured in the energy range 636-658 eV consisting of both Mn2p<sub>3/2</sub> and Mn2p<sub>1/2</sub> core levels. For all

measured samples we have observed both Mn<sup>3+</sup> and Mn<sup>4+</sup> oxidation states (Supplementary data Fig. 4B) with BE of 640.4 eV and 642.0 eV, respectively. The small satellite structure with BE of ca. 644.0 eV also proves the presence of Mn<sup>4+</sup> ions on the surface, according to the curve fitting procedure [33]. Mn<sup>4+</sup> predominates on the surface in all samples containing manganese and its concentration increases with increasing Mn loading (see Table 3). The only manganese containing sample before catalytic activity test differs from this behavior showing predominance of Mn<sup>3+</sup> ions on the surface. From the XPS analysis it is visible, that with increasing of the amount of manganese the relative abundance of Co<sup>3+</sup> ions sharply decrease and Co<sup>2+</sup> is only species in the sample with highest Mn concentration (see Table 3). The same tendency was observed in our previous investigations regarding bi-component Co-Mn catalysts supported on SiO<sub>2</sub> [17] or bulk Co-Mn mixed oxide [34]. According to the authors of ref. [35], the doping of manganese into the spinel structure of cobalt oxide increased crystal defects, which probably caused the increase in the amount of octahedrally coordinated divalent cobalt cations that are responsible for catalytic activity. El-Shobaky et al. [36] explained the increase in the lattice constant of Co<sub>3</sub>O<sub>4</sub> after incorporation of manganese with the conversion of some Co<sup>3+</sup> into Co<sup>2+</sup>.

After the *n*-hexane oxidation reaction, one can summarize the results from XPS – investigation as follows:

- The Co2p<sub>1/2</sub>/Mn2p ratio on the surface of the samples 1Co0.5Mn-SBA-15 and 1Co1Mn-SBA-15 decreases demonstrating enrichment in the Mn component. The opposite trend is observed for the 1Co2Mn-SBA-15 material.
- The Co/Si ratio decreases insignificantly for all cobalt containing samples, except for the 1Co2Mn-SBA-15 where it is increased. The ratio between different cobalt species (Co<sup>2+</sup>/Co<sup>3+</sup>) varies depending on the manganese content - it increases about three times for 1Co0.5Mn-SBA-15 and it changes insignificantly for 1Co1Mn-SBA-15. For the sample, in which before the reaction (1Co2Mn-SBA-15) the cobalt was present mainly as Co<sup>2+</sup>, part of it was oxidized to Co<sup>3+</sup>.
- The concentration of Mn<sup>4+</sup> on the surface of 1Co0.5Mn-SBA-15 increases by 68% and that of Co<sup>2+</sup> by 75%. These very close values could be explained by the electronic transfer between Co and Mn according the following equation:



It can be expected that in the Mn<sub>x</sub>Co<sub>3-x</sub>O<sub>4</sub> solid solution, the electron transfer between Co<sup>2+</sup> and Mn<sup>4+</sup> could occur [37]. Thus, a part of Co<sup>3+</sup> and Mn<sup>3+</sup> might be converted into Co<sup>2+</sup> and Mn<sup>4+</sup>. The formation of Mn-Co solid solution is confirmed by TEM and XRD measurements.

The wide-angle XRD pattern (Fig. 6) of the 2Co-SBA-15 material presents low and broad peaks corresponding to crystalline Co<sub>3</sub>O<sub>4</sub> phase (Card N 01-071-4921). Concerning the Mn-SBA-15 material, the wide-angle XRD pattern exhibits low and broad peaks indicating the coexistence of the phases MnO<sub>2</sub> Pyrolusite (card N° 01-071-4824) and Mn<sub>2</sub>O<sub>3</sub> Bixbyite (Card N°00-041-1442). The broad line at a slightly lower 2θ angle (2θ =36,5) in comparison with that of single component cobalt is observed with the bi-component Co-Mn samples indicating Co-Mn mixed oxide formation, a loss of crystallinity and decrease in the particle size [17]. The particle size calculation using the reflection at 2θ=36.5, coming from the [311] plane, decreases from 15 nm for mono-component cobalt down to 4 nm for bi-component Co:Mn samples. The decomposition of supported mixed cobalt and manganese nitrates at low

temperatures (250–400 °C) often produces finely divided non-stoichiometric spinels. In order to verify this hypothesis and to determine whether the solid solution corresponds to Mn inserted into  $\text{Co}_3\text{O}_4$  or to Co inserted into  $\text{Mn}_3\text{O}_4$ , electron diffraction was applied. The obtained electron diffraction micrograph was compared with the electron micrographs of  $\text{Co}_3\text{O}_4$  and  $\text{Mn}_3\text{O}_4$  from ICDD data base (cards N° 03-065-3103 and N° 00-024-0734, respectively) and it was found out to be similar to the one of  $\text{Co}_3\text{O}_4$  (Fig 7). This comparison is in agreement with the formation of solid solutions  $\text{Mn}_x\text{Co}_{3-x}\text{O}_4$  corresponding to Mn inserted into  $\text{Co}_3\text{O}_4$  phase [38].

After the n-hexane oxidation the XRD patterns (Fig. 5 Supplementary data) of mono component Co-SBA-15, Mn-SBA-15 and bi-component CoMn-SBA-15 materials are similar to those before reaction indicating that crystalline phases are not affected.

The TPR profiles of all samples are shown in Figure 8. Three reduction peaks are visible in the TPR spectra of mono component cobalt sample. The first two at 324 and 354 °C are attributed to the reduction of large size supported  $\text{Co}_3\text{O}_4$  particles [17]. The third one, which is centered at 481°C, is to be ascribed to small particles strongly interacting with the support [21]. As it was shown by TEM the large nanoparticles were located inside the nanochannels and composed of small nanoparticles in adjacent channels due to the micropores in the walls of SBA-15. The reduction profiles of the single component manganese samples correspond to the two-step reduction of  $\text{Mn}_3\text{O}_4$  ( $\text{MnO}_2 \rightarrow \text{Mn}_3\text{O}_4 \rightarrow \text{Mn}_3\text{O}_4$ ;  $\text{Mn}_3\text{O}_4 \rightarrow \text{MnO}$ ) [33].

The Co-Mn catalysts start their reduction process at lower temperature comparing with the mono component one. For all bi-component samples, three reduction peaks are visible. According to the authors of ref. [15] the hydrogen consumption at lowest temperature can be associated with easily reducible highly dispersed surface  $\text{Mn}^{4+}$  species coming from by nano Co-Mn oxide and adsorbed oxygen species ( $\text{Co}_x\text{Mn}_y\text{O}_z$  (s)+ $\text{H}_2$ (g) $\rightarrow$   $\text{Mn}_3\text{O}_4$  -  $\text{Co}_3\text{O}_4$  (s) +  $\text{H}_2\text{O}$ (g)). The second reduction band could be ascribed to the reduction of  $\text{Mn}_3\text{O}_4$  and  $\text{Co}_3\text{O}_4$  ( $\text{Mn}_3\text{O}_4$ - $\text{Co}_3\text{O}_4$  (s)+ $\text{H}_2$ (g) $\rightarrow$   $\text{MnO}$ - $\text{CoO}$ (s) +  $\text{H}_2\text{O}$ (g)) [39, 40]. The third step is to be assigned to reduction of  $\text{Co}^{2+}$  to metallic cobalt since the process of  $\text{Mn}^{2+} \rightarrow \text{Mn}^0$  needs temperature higher than 1200°C [41]. As can be seen, the modification with manganese leads to a shift of the three reduction peaks to a lower temperature, indicating that the reduction of the samples increases. The highest shift is observed for the sample with the smallest quantities of manganese – 1Co0.5Mn-SBA-15, which indicates that it is with best reduction properties among all two component catalysts.

The  $\text{O}_2$ -TPD experiment was performed in order to obtain information about the type of oxygen species on the surface of the studied catalyst samples. Three desorption regions are observed in the  $\text{O}_2$ -TPD spectra: 50-170 °C, 200-300 °C and 300-425 °C (Figure 9). According to the current literature the lower temperature desorption peak (< 200°C) is ascribed to desorption of physically adsorbed oxygen. The desorption of chemisorbed oxygen occurs at 200°C to 400°C, while the desorption at higher temperatures (> 400 °C) corresponds to the bulk lattice oxygen in the structure [42, 43]. Song et al. [44] have classified the oxygen desorption peaks for mesoporous cobalt oxides as follows:

- desorption of surface adsorbed peroxy  $\text{O}_2^-(\text{ad})$  species within 150–250°C interval;
- desorption of surface adsorbed  $\text{O}^-(\text{ad})$  species within the interval 280–340 °C;
- desorption of surface lattice oxygen  $\text{O}^{2-}(\text{ad/lattice})$  within the interval 350–670 °C; and beyond 700 °C appears the desorption of bulk lattice oxygen.

By comparing our results with the data in the literature, we can ascribe the TPD peak in the T1 region to desorption of physically adsorbed oxygen in the T2 to the  $\text{O}_2^-(\text{ad})$  species

and in the T3 interval to the  $O^-(ad)$  species. As can be seen from the figure, the oxygen continues to desorb above 400 °C for the catalyst with 0.5 mol manganese (1Co0.5Mn-SBA-15). According to the literature, this form of adsorbed oxygen can be related to the surface lattice oxygen  $O^{2-}(ad/lattice)$ . If we compare the  $O_2$ -TPD spectra of the monocomponent cobalt sample with that of the two component Co-Mn, it is visible that the doping of cobalt oxide with manganese shifts desorption peaks in the T2 interval to the lower temperature, revealing the greater mobility of the  $O_2^-(ad)$  species. Only the sample 1Co0.5Mn-SBA-15 shows desorption of oxygen from the surface lattice at temperatures lower than 450 °C. As the experiment was terminated at 450° (temperature at which 100% conversion for all tested compounds was observed) for other catalysts most likely that desorption is performed at higher temperatures. The shifts of the desorption peaks in the intervals T2 and T3 to the lower temperature could be explained by the loss of crystallinity (as it was shown by XRD data) and as a result an increase in the number of vacancies due to structural defects. These vacancies can provide centers for adsorption of oxygen [8, 45]. The concentration of  $Co^{2+}$  ions on the surface of two component samples is increased as was revealed from XPS data (seen on Fig. 3).  $Co^{2+}$  ions can be centres for oxygen adsorption and formation of active oxygen species which are a prerequisite for catalytic oxidation [47]. The correlation between catalytic activity in toluene combustion and surface  $Co^{2+}$  concentration was demonstrated by E. Genty and co-authors [8].

Based on the results discussed in this section it can be concluded that:

- The main phase for a single component cobalt sample is  $Co_3O_4$ . The co-existence of two types of  $Co_3O_4$  particles could be assumed: large supported  $Co_3O_4$  particles and small particles strongly interacting with the support. The particle clusters of  $Co_3O_4$  are on the surface and they are partially located inside the pore system of SBA-15. The  $Co^{3+}$  is the only species on the Co-SBA-15 surface.
- $MnO_2$  (pyrolusite) and  $Mn_2O_3$  (bixbyite) are formed in a single component Mn catalyst supported on the SBA-15. The oxide particles are mostly located inside the channels of SBA-15 filling them up, leading to a substantial drop in the surface area and in the pore volume.
- The doping of cobalt oxide with Mn leads to: (1) Formation of finely divided oxides. (2) Higher oxygen mobility in the bi-component Co-Mn samples. The sample with highest mobility of the surface adsorbed  $O_2^-(ad)$  and surface lattice oxygen species is that with 0.5 mol manganese (1Co0.5Mn-SBA-15). (3) Upon increasing the amount of Mn the relative abundance of  $Co^{2+}$  ions on the surface increases.

### 3.2. Catalytic activity

The temperature dependencies of the CO, propane and *n*-hexane complete oxidation over the mono- and bi-component catalysts are shown in Figure 11.  $H_2O$  and  $CO_2$  were the only detectable reaction products of VOC oxidation on all investigated samples. The only detectable product of incomplete oxidation was CO at concentration range below 10 ppm.

As it is evident in Figure 10, the order of activity depends on the reaction compound.

In the cases of complete oxidation of propane and CO, the mono-component cobalt sample is the most active. These data are consistent with results in literature relating to the oxidation of these compounds in the presence of cobalt catalysts. It is widely accepted that the  $Co^{3+}$  species on the surface of  $Co_3O_4$  are the reactive sites or centres for CO oxidation [7, 48]. As it was shown above, the only surface species on the Co-SBA-15 surface is  $Co^{3+}$ . Comparing the order of activities in CO oxidation reaction (Figure 10A) and the Table 3, it

can be noticed that the activity is decreasing with decrease in the  $\text{Co}^{3+}$  surface concentration and it is lowest at 1Co2Mn-SBA-15 catalyst, in which the cobalt is present in the form of the surface  $\text{Co}^{2+}$ . Quite similar is the situation in the case of propane oxidation: the most active sample is the mono component cobalt catalyst and with increasing the manganese concentration in the samples, the catalytic activity drops down. The most active catalyst among the bi-component samples is the one having Co:Mn=1:0.5 molar ratio.

In the reaction of *n*-hexane oxidation, the catalyst displaying highest activity is the Co1Mn0.5-SBA-15 sample and the lowest activity is shown by the monocomponent Mn-SBA-15. The catalytic activity of the other two bi-component Co-Mn samples is a comparable with that of mono-component cobalt one. In our previous investigation concerning bi-component CoMn samples, supported on  $\text{SiO}_2$ , we established that the *n*-hexane oxidation reaction proceeds through Mars -van Krevelen mechanism [33]. According to this mechanism the VOCs are oxidized by the solid and the oxygen species introduced in the organic molecule come from the crystal lattice. Thus, the catalytic behavior can be correlated with the lattice oxygen mobility and with the corresponding the catalyst reducibility. It has been established that high concentration of surface oxygen species is important for achieving high activity in propane [49, 50] and toluene oxidation reactions over  $\text{Co}_3\text{O}_4$  containing catalysts [8].

The mono component manganese catalyst exhibits the lowest activity in all the studied reactions. One possible explanation is that the manganese oxides are situated in the mesoporous channels, which very likely result in a less accessible active manganese sites in this sample.

According to the applied physicochemical methods after the reaction of *n*-hexane oxidation it was established that insignificant changes occur in the mesoporous structure and morphology, oxide particle size and oxide phases. Probably the mesoporous structure prevents the agglomeration of the oxide particles after the reaction. An increase in the average particle size about twice was registered when Co-Mn oxides are supported on  $\text{SiO}_2$  [17].

#### **4. Conclusions**

It was found that the modification of SBA-15 by “two-solvent” technique with Co, Mn or simultaneously with both cobalt and manganese does not change significantly the mesoporous structure, however its pores are partially blocked by the oxides, resulting in the decrease in the specific surface area and in the pore volume. In the case of mono component Co-SBA-15, the clusters of  $\text{Co}_3\text{O}_4$  are on the surface and they are partially located inside the pore system of SBA-15 while for Mn-SBA-15 sample, the oxide phases preferentially fill up the channels of SBA-15 forming nanowires. The mixed oxide nanowires are formed in the channels of CoMn-SBA-15 material along with small nanoparticles, aggregated outside of the channels.

The mesoporous structure and morphology of SBA-15, type of oxide phases and the size of the oxide particles remain almost unchanged after tests in reaction of complete *n*-hexane oxidation and this is valid for all studied samples. The observed resistance towards agglomeration can be attributed to the role of the mesoporous structure. On the other hand, after reaction the surface concentration of different cobalt and manganese species undergoes significant changes, except for the sample with equimolar Co:Mn ratio.

In the cases of complete oxidation of propane and CO, the mono-component cobalt sample is the most active due to the presence of only  $\text{Co}^{3+}$  species on the surface. The sample with Co:Mn molar ratio of 1:0.5 is most active in the *n*-hexane combustion. It exhibits the highest activity among the synthesized bi-component samples in all studied reactions which is

explained by the formation of finely divided oxides, highest reducibility and highest mobility of the surface and lattice oxygen.

***Acknowledgment:** The authors thank the Bulgarian Science Fund for financial support under Contracts DNTS/France/01/5 and Franco - Bulgarian project RILA 38651RJ.*

## References

- [1] J. Spivey, in: G. C. Bond, G. Webb, *Catalysis*, 8 (1989) 157–203.
- [2] M. Baldi, E. Finocchio, F. Milella, G. Busca, *Appl. Catal. B: Environ.*, 16 (1998) 43–51.
- [3] R. Craciun, B. Nentwick, K. Hadjiivanov, H. Knozinger, *Appl. Catal. A: Gen.*, 243 (2003) 67–79.
- [4] Y. F. Chang, J.G. McCarty, *Catal. Today*, **30** (1996) 163–170.
- [5] L. F. Liotta, H. Wu, G. Pantaleo, A.M. Venezia, *Catal. Sci. Technol.* 3 (2013) 3085–3102.
- [6] H. Huang, Y. Xu, Q. Feng, D.Y.C. Leung, *Catal. Sci. Technol.* 5 (2015) 2649–2669.
- [7] J. Carpentier, S. Siffert, J. F. Lamonier, H. Laversin, A. Aboukais; *J. Por. Mat.* 14 (2007) 103–110
- [8] E. Genty, J. Brunet, C. Poupin, S. Casale, S. Capelle, P. Massiani, S. Siffert, and R. Cousin; *Catalysts* 5 (2015) 851–867
- [9] L. F. Liotta; X. W. Xie, Y. Li, Z. Q. Liu, M. Haruta and W. J. Shen, *Nature* 458 (2009) 746–749.
- [10] H. F. Wang, R. Kavanagh, Y. L. Guo, Y. Guo, G. Z. Lu and P. Hu, *J. Catal.* 296 (2012) 110–119.
- [11] V. G. Milt, M. A. Ulla, E. A. Lombardo, *J. Catal.* 200 (2001) 241–249.
- [12] A. Torncrona, M. Skoglundh, P. Thormählen, E. Fridell, E. Jobson, *Appl. Catal. B: Environ.* 14 (1997) 13–22.
- [13] Á. Szegedi, M. Popova, A. Dimitrov, Z. Cherkezova-Zheleva, I. Mitov, *Micropor Mesopor Mat*, 136 (2010) 106–114.
- [14] F. Wyrwalski, J.-F. Lamonier, S. Siffert, A. Aboukais, *Appl. Catal. B: Environ.* 70 (1–4) (2007) 393–399
- [15] X. Zhang, J. Yea, J. Yuan, T. Cai, B. Xiao, Z. Liu, K. Zhao, L. Yang, D. He, *Appl. Catal. A: Gen.* 566 (2018) 104–112.
- [16] M. Haidy C, R. Molina, S. Moreno, *Appl. Catal. A: Gen* 492 (2015) 48–59.
- [17] S. Todorova, H. Kolev, J. P. Holgado, G. Kadinov, Ch. Bonev, R. Pereñíguez, A. Caballero, *Appl. Catal. B: Environ.* 94 (2010) 46–54.
- [18] Todorova, I. Yordanova, A. Naydenov, H. Kolev, Z. Cherkezova-Zheleva, K. Tenchev, B. Kunev, *Rev. Roum. Chim.* 59 (2014) 259–265.
- [19] S. Sadjadi, M.M. Heravi, *RSC. Adv.* 7 (2017) 30815–30838.
- [20] Z. Xiao-Dong, W. Yin, Y. Yi-Qiong, C. Dan, *Acta Phys. - Chim. Sin.* 31 (2015) 1633–1646.
- [21] T. Tsoncheva, L. Ivanova, J. Rosenholm, M. Linden, *Appl. Catal. B: Environ.* 89 (2009) 365–374.
- [22] T. Tsoncheva, J. Rosenholm, C.V. Teixeira, M. Dimitrov, M. Linden, C. Minchev, *Micropor Mesopor Mat.* 89 (2006) 209–218.
- [23] T. Tsoncheva, G. Issa, T. Blasco, M. Dimitrov, M. Popova, S. Hernández, D. Kovacheva, G. Atanasova, J. M. López Nieto, *Appl. Catal. A: Gen.* 453 (2013) 1–12.
- [24] R. Ivanova, I. Genova, D. Kovacheva, G. Atanasova, T. Tsoncheva; *J. Por. Mat.*, 23 (2016) 1005–1013.
- [25] A. Galarneau, M. Nader, F. Guenneau, F.A. Di Renzo, *J. Phys. Chem. C* 111 (2007) 8268–8277.

- [26] M. Imperor-Clerc, D. Bazin, M-D Appay, P. Beaunier and A. Davidson, *Chem. Mater.* (2004) 16 (9) 1813–1821.
- [27] S. Brunauer, P.H Emmet, E. Teller, *J. Am. Chem. Soc.* 60 (1938) 309–31.
- [28] E.P. Barrett, L.G. Joyner, P.P. Halenda, *J. Am. Soc.* 73 (1951) 373–380.
- [29] M. Thommes, K. Kaneko, A. V. Neimark, J. P. Olivier, F. Rodriguez-Reinoso, J. Rouquerol, K. S. W. Sing, *Pure Appl. Chem.* 87(9-10) (2015) 1051–1069.
- [30] S. Zhu, Z. Zhou, D. Zhang, H. Wang, *Micropor. Mesopor. Mat.* 95 (2006) 257–264.
- [31] Q. Q. Xu, G. Xu, J.Z. Yin, A. Q. Wang, Y. L. Ma, J. J. Gao, *Ind. Eng. Chem. Res.* 53 (2014) 10366-10371.
- [32] Y. Belmoujahid, M. Bonne, Y. Scudeller, D. Schleich, Y. Grohens, B. Lebeau, *Micropor Mesopor Mat* 201 (2015) 124–133.
- [33] S. Todorova, A. Naydenov, H. Kolev, J. P. Holgado, G. Ivanov; G. Kadinov, A. Caballero, *Appl. Catal. A: Gen.* 414 (2012) 43–51.
- [34] I. D. Yordanova, S. Zh. Todorova, H. G. Kolev, Z. P. Cherkezova-Zheleva, *Bul. Chem. Comm.* 49 (2017) 99–104.
- [35] J. Li , Xi Liang, S. Xu, J. Hao, *Appl. Catal. B: Environ.* 90 (2009) 307–312.
- [36] H. G. El-Shobaky, M.A. Shouman, A.A. Attia, *Colloid. Surf. A: Physicochem. Eng. Aspects* 274 (2006) 62–70.
- [37] Q. Zhang, X. Liu, W.g Fan, Y. Wang, *Appl. Catal. B: Environ.* 102 (2011) 207–214.
- [38] R. M. Rojas, E. Vila, O.Garcia and J. L. Martin de Vidales, *J. Mater. Chem.* 4(10) (1994) 1635–1639.
- [39] W. Tang, W. Li, D. Li, G. Liu, X. Wu, Y. Chen, *Catal. Lett.* 144 (2014) 1900–1910.
- [40] J.Y. Luo, M. Ming, L. Xiang, X.G. Li, Y.Q. Zha, T.D. Hu, Y.N. Xie, Z. Jing, *J. Catal.* 254 (2008) 310–324.
- [41] G. Zhou, X. He, S. Liu, H. Xie, M. Fu *J. Ind. Eng. Chem.* 21 (2015) 932–941.
- [42] X. Zhang, J. Ye, J. Yuan, T. Cai, B. Xiao, Z. Liu, K. Zhao, L. Yang, D. He, *Appl. Catal. A: Gen.* 566 (2018) 104–112.
- [43] X. Liu, Q. Liu, X.G. Huang, X.L. Nie, Z. Huang, *J. Chin. Chem. Soc.* 61 (2014) 490–494.
- [44] W. Song, Al. S. Poyraz, Y. Meng, Z. Ren, S.-Y. Chen and S. L. Suib, *Chem. Mater.* 26 (2014) 4629–4639.
- [45] M.R. Morales, B.P. Barbero, L.E. Cadús, *Fuel* 87 (2008) 1177–1186.
- [47] J. Łojewska, A. Kołodziej, J. Żak, J. Stoch, *Catal. Today* 105 (2005) 655–661.
- [48] B. Faure and P. Alphonse, *Appl. Catal. B: Environ.* 180 (2016) 715–725.
- [49] Q. Liu, L.-C. Wang, M. Chen, Y. Cao, H.-Y.He, K.-N.Fan, *J. Catal.* 263 (2009) 104–113.
- [50] T. Garcia, S. Agouram, J.F. Sanchez-Royo, R. Murillo, A.M. Mastral, A. Aranda, I. Vazquez, A. Dejoz, B. Solsona, *Appl. Catal. A: Gen.* 386 (2010) 16–27.

### ***Figure captions***

**Figure 1.** SAXS patterns of the catalysts before (A) and after (B) reaction.

**Figure 2.** TEM images of (a, b) Co-SBA-15, (c, d) Mn-SBA-15 and (e, f) 1Co1Mn-SBA-15 catalysts before reaction

**Figure 3.** TEM images in darkfield mode of (a) Co-SBA-15 with EDX Co element mapping (b), (c) Mn-SBA-15 with EDX Mn element mapping (d) and (e) 1Co1Mn-SBA-15 with EDX Co (f) and Mn (g) element mappings before reaction.

**Figure 4.** Nitrogen adsorption-desorption isotherms of the catalysts before (A) and after *n*-hexane oxidation (B).

**Figure 5.** Mesopore size distribution of the catalysts before (A) and after (B) after *n*-hexane oxidation.

**Figure 6.** Wide angles X-ray diffraction patterns of the catalysts before reaction (the triangles correspond to  $\text{Co}_3\text{O}_4$  reflections, the squares to Pyrolusite ( $\text{MnO}_2$ ) and the stars to Bixbyite ( $\text{Mn}_2\text{O}_3$ ) reflections).

**Figure 7.** Electron diffraction pattern of 1Co1Mn-SBA-15 (a) and electron diffraction patterns of (b)  $\text{Co}_3\text{O}_4$  (card n°03-065-3103) and (c)  $\text{Mn}_3\text{O}_4$  from ICDD data base (card n°00-024-0734).

**Figure 8.** TPR spectra of single- and bi-component catalysts.

**Figure 9.**  $\text{O}_2$ -TPD profiles of single- and bi-component catalysts.

**Figure 10.** Temperature dependence of A. CO oxidation; B. propane and combustion; C. *n*-hexane combustion.

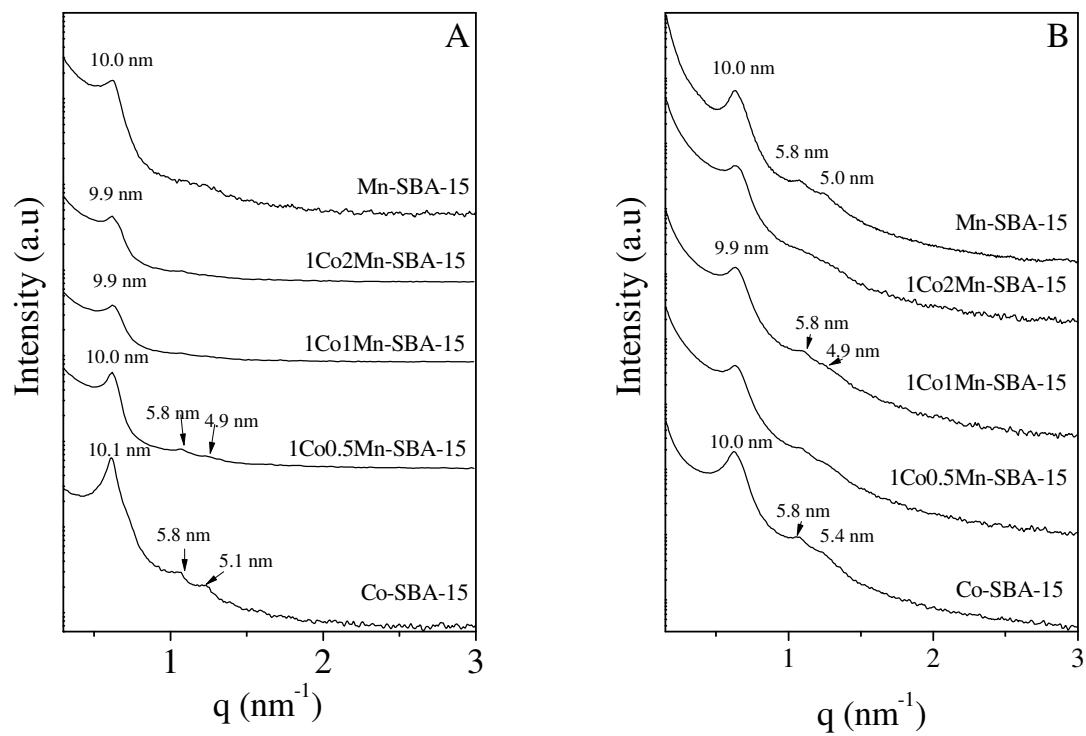


**Figure 1**

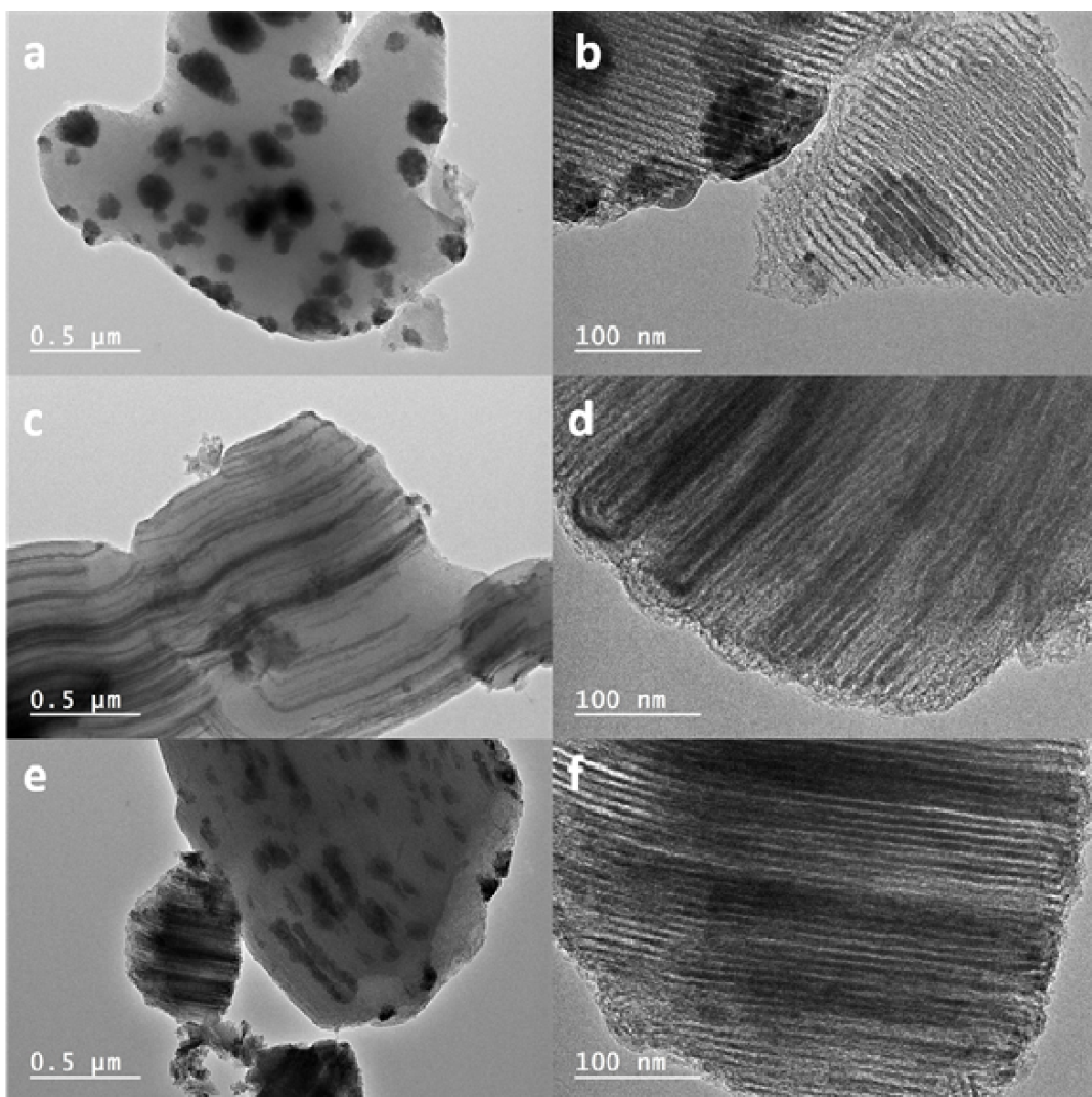


**Figure 2.**

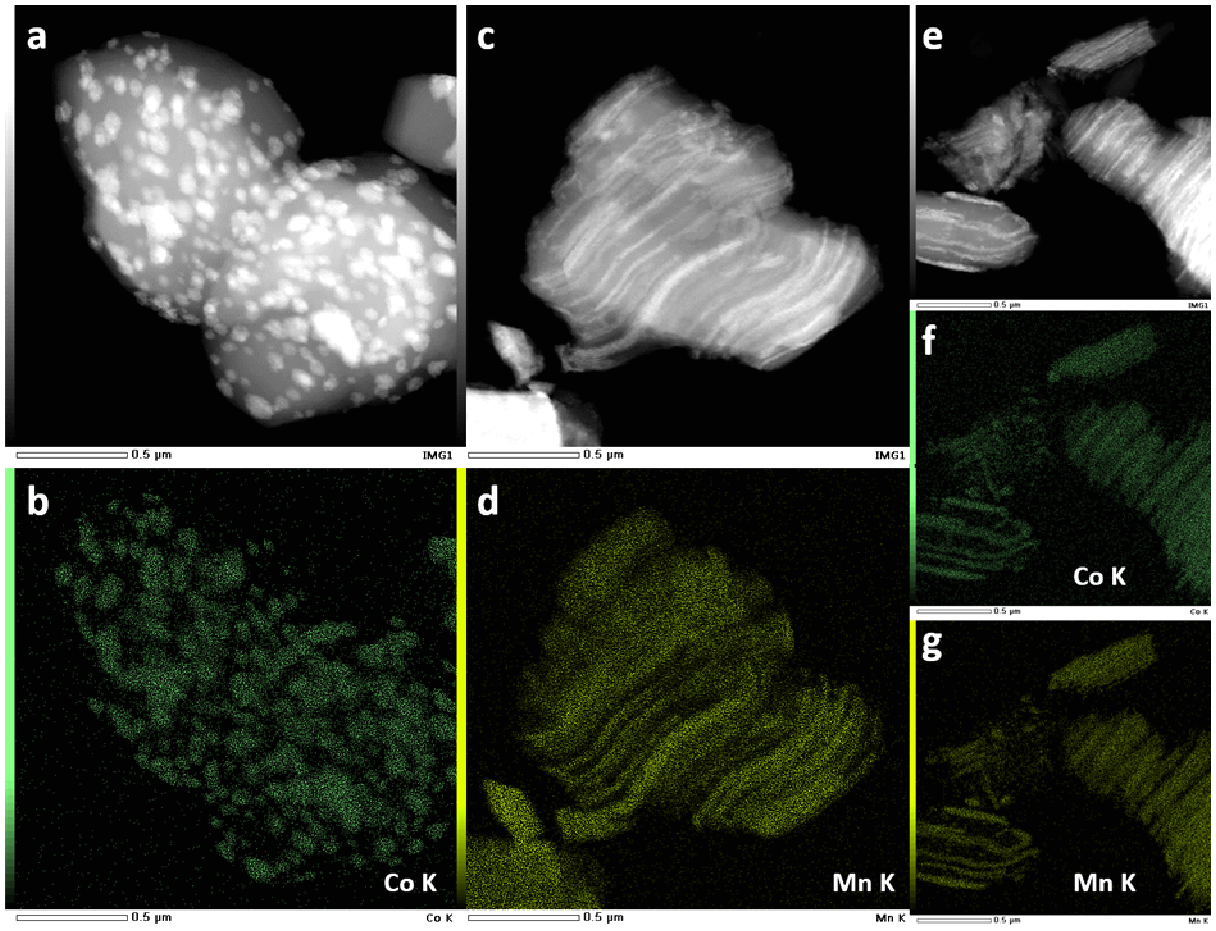


Figure 3:

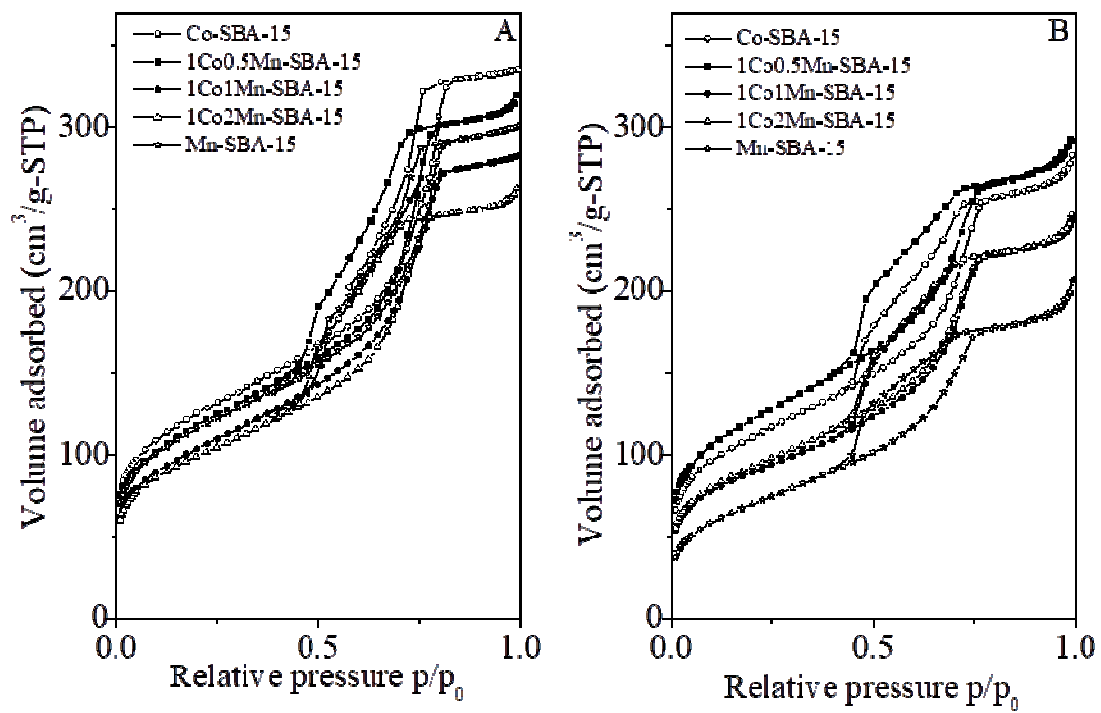


Figure 4.

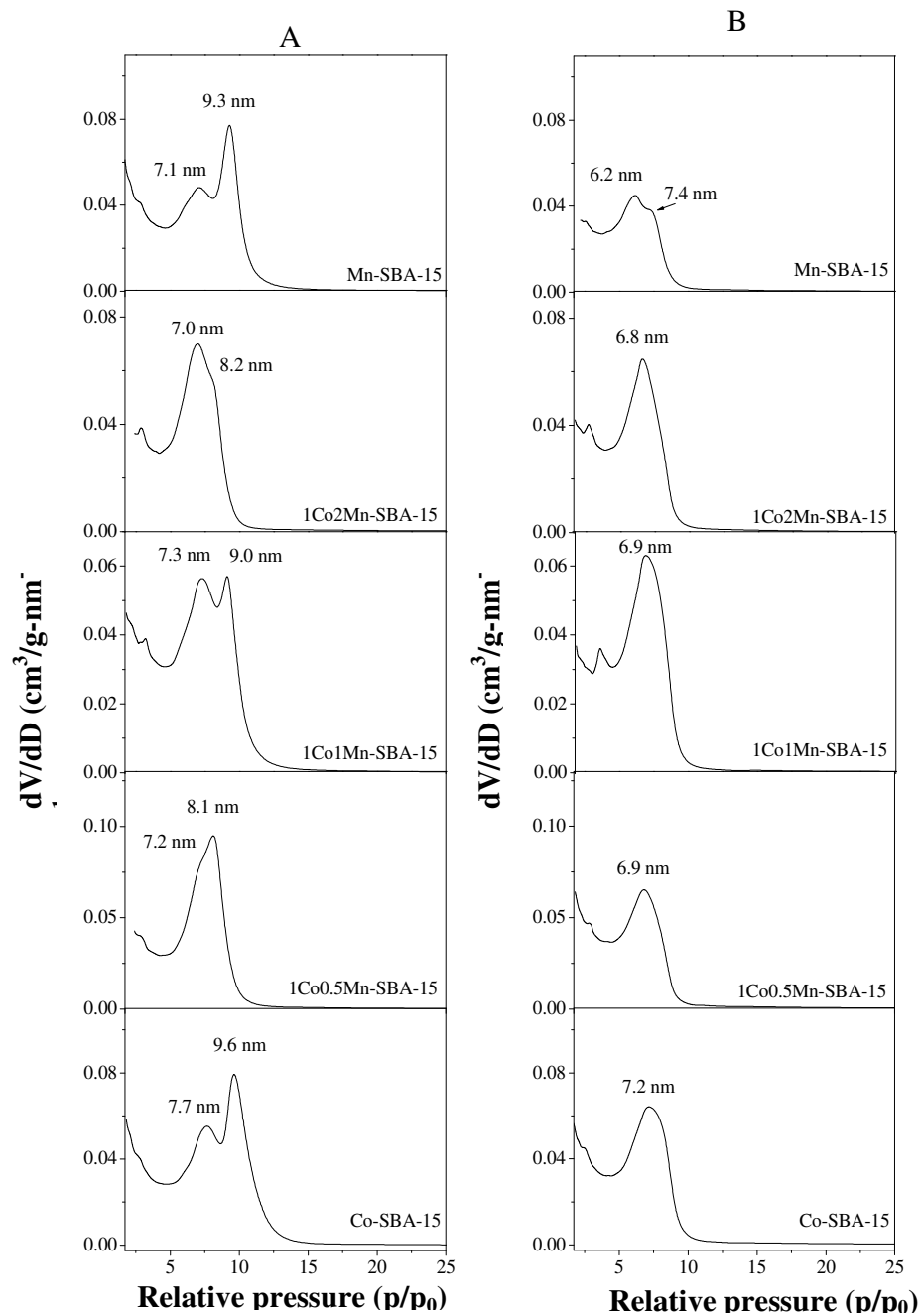


Figure 5.

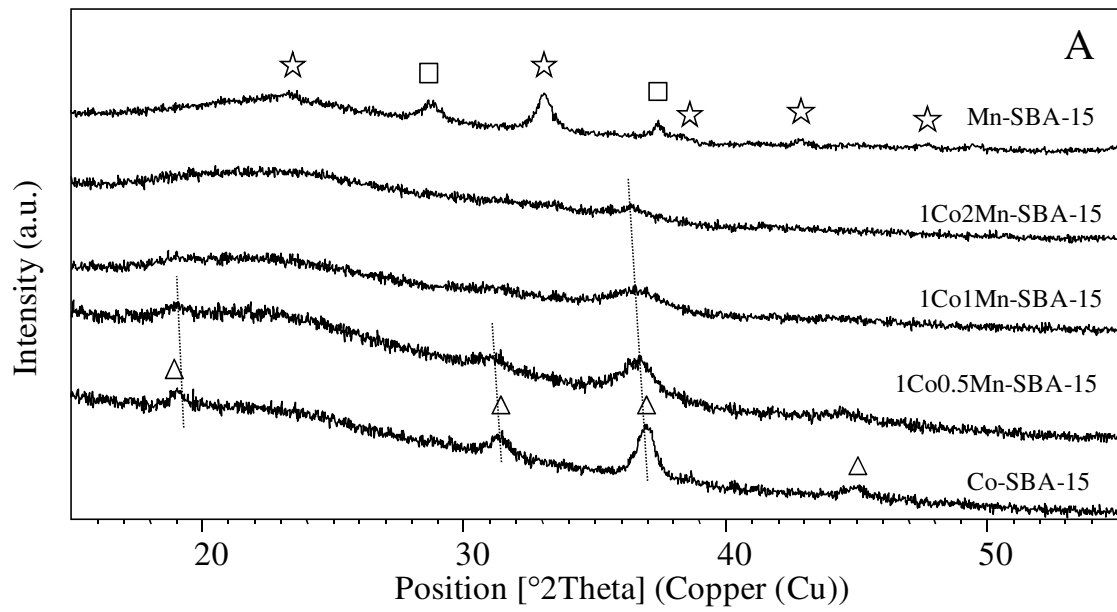


Figure 6.

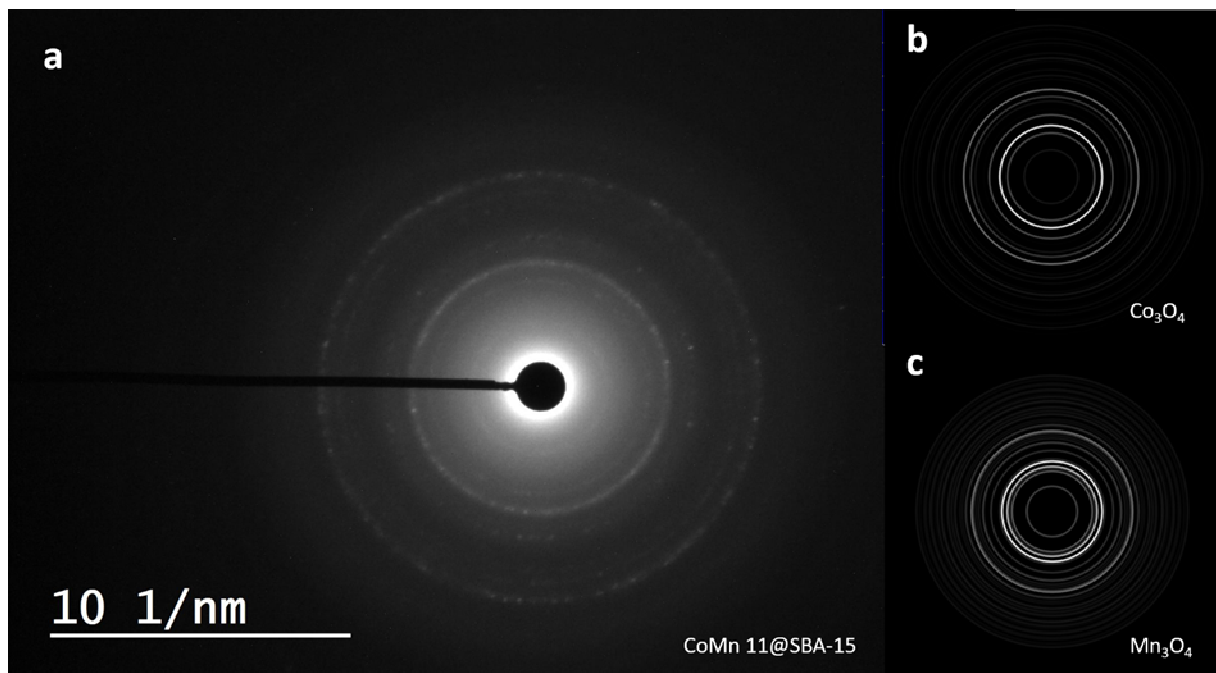
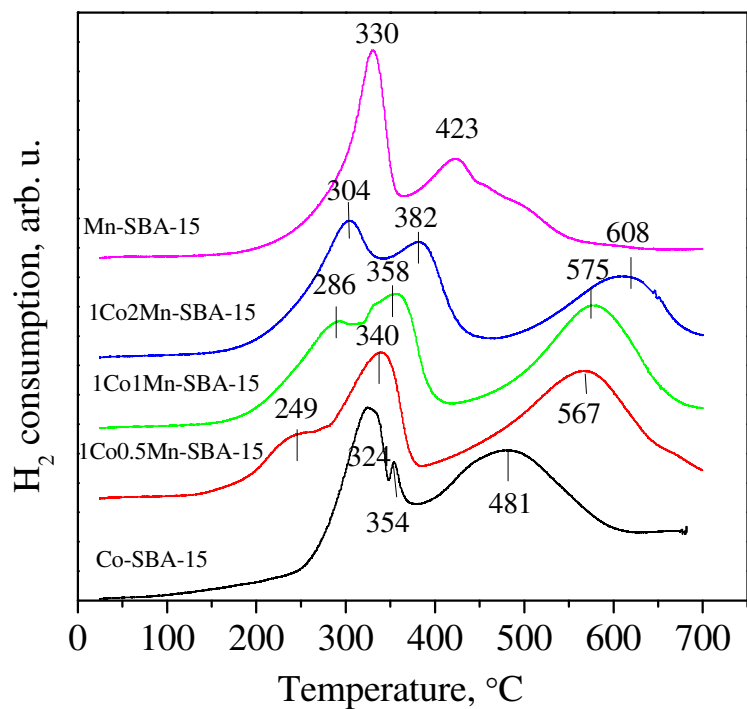
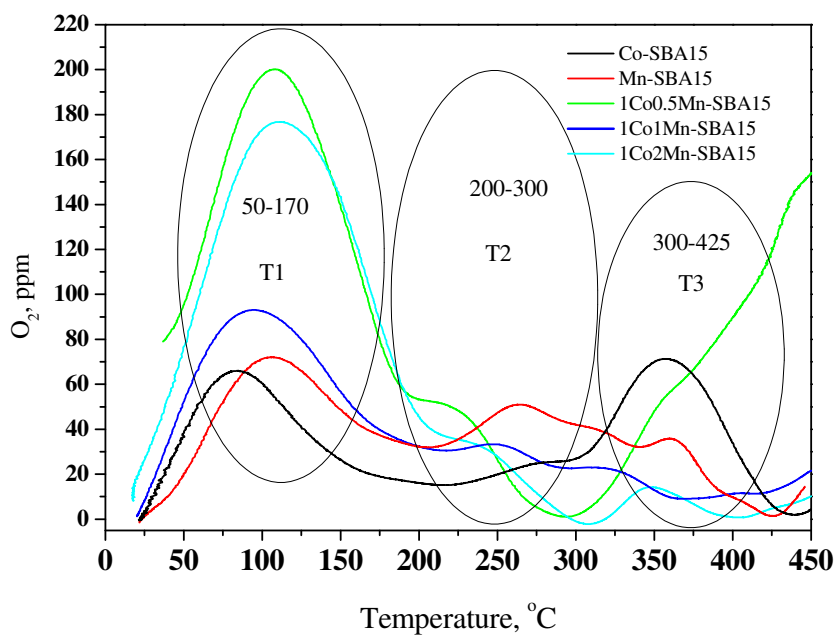


Figure 7.



**Figure 8**



**Figure 9.**

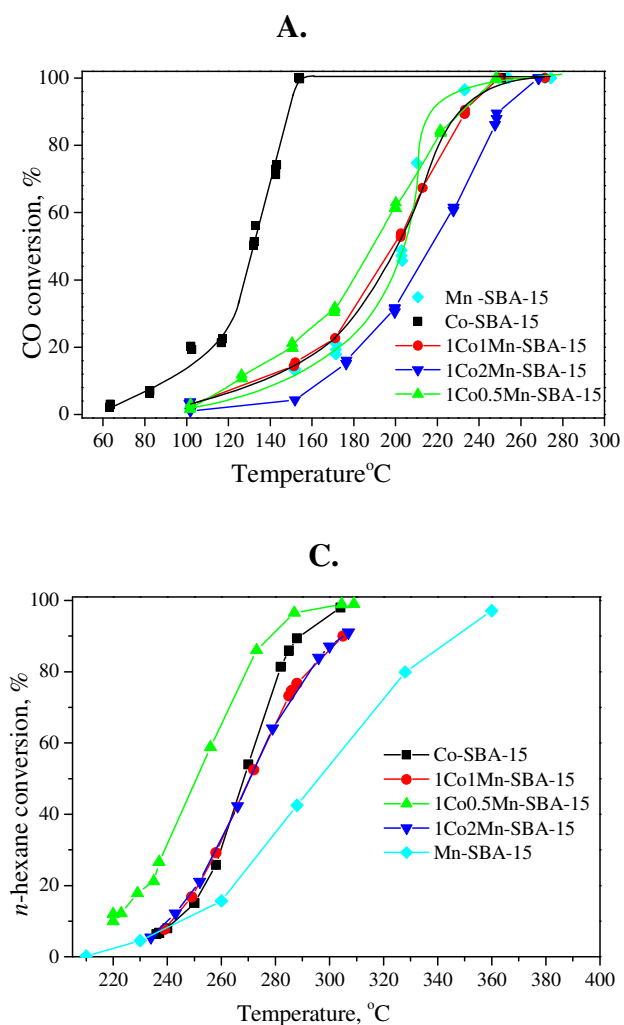


**Figure 10.**

Table 1: EDX elemental Co and Mn composition (% atomic) of the Co-SBA-15, Mn-SBA-15 and 1Co1Mn-SBA-15 materials before (BR) and after n-hexane oxidation (AR)

Sample	Co	Mn	Si
Co-SBA-15 BR	7.35 ± 0.34	0	27.39 ± 0.60
Co-SBA-15 AR	6.89 ± 1.00	0	26.80 ± 1.08
Mn-SBA-15 BR	0	8.00 ± 0.44	26.86 ± 0.26
Mn-SBA-15 AR	0	8.20 ± 1.01	25.84 ± 0.81
1Co1Mn-SBA-15 BR	3.45 ± 0.20	4.13 ± 0.15	27.31 ± 0.42
1Co1Mn-SBA-15 AR	3.52 ± 0.16	4.17 ± 0.27	27.41 ± 0.38

Table 2: d-spacing values, specific surface area ( $S_{BET}$ ), pore volume ( $V_p$ ) and pore diameter ( $\varnothing$ ) of the catalysts before and after reaction (n-hexane oxidation)

Sample		d-spacing (nm)	$S_{BET}$ (m <sup>2</sup> /g)	$V_p^*$ (cm <sup>3</sup> /g-STP)	$\varnothing^{**}$ (nm)
Co-SBA-15	Before reaction	10.1	439	0.52	7.2-9.6
	After reaction	10.0	389	0.44	7.2
1Co0.5Mn-SBA-15	Before reaction	10.0	416	0.49	7.2-8.1
	After reaction	10.0	426	0.45	6.9
1Co1Mn-SBA-15	Before reaction	9.9	366	0.44	7.3-9.0
	After reaction	10.0	314	0.38	6.9
1Co2Mn-SBA-15	Before reaction	9.9	349	0.41	7.0-8.2
	After reaction	10.0	326	0.38	6.8
Mn-SBA-15	Before reaction	10.0	403	0.46	7.1-9.3
	After reaction	10.0	253	0.25	6.2-7.4

\* Single point values

\*\* Values obtained from BJH method applied to the adsorption branch of the isotherm

**Table 3.** Surface atomic concentrations (at. %) of  $Co^{2+}$ ,  $Co^{3+}$ ,  $Mn^{3+}$  and  $Mn^{4+}$  ions of the investigated sample surfaces before and after catalytic test (catalytic test is n-hexane complete oxidation).

	before		after		before		after		before	after	before	after	before	after
	$Mn^{3+}$	$Mn^{4+}$	$Mn^{3+}$	$Mn^{4+}$	$Co^{2+}$	$Co^{3+}$	$Co^{2+}$	$Co^{3+}$	Co/Si	Co/Si	Mn/Si	Mn/Si	$Co2p_{1/2}/Mn2p$	$Co2p_{1/2}/Mn2p$
<b>Co-SBA-15</b>	-	-	-	-	0	1.22	0.26	1.10	0,032	0,035			-	-
<b>1Co0.5Mn-SBA-15</b>	0.27	0.38	0.26	0.64	0.28	0.55	0.49	0.35	0,022	0,023	0,017	0,025	1.29	1.04
<b>1Co1Mn-SBA-15</b>	0.30	0.78	0.44	0.71	0.37	0.39	0.35	0.36	0,02	0,018	0,047	0,031	0.70	0.61
<b>1Co2Mn-SBA-15</b>	0.65	0.94	0.32	0.71	0.51	0	0.28	0.50	0,014	0,022	0,044	0,028	0.32	0.76
<b>Mn-SBA-15</b>	1.98	1.32	0.48	1.19	-	-	-	-			0,09	0,046	-	-